Comparison of Breathing and Spoke Mode Strength in the H6 Hall Thruster Using High Speed Imaging

IEPC-2013-353

Presented at the 33^{rd} International Electric Propulsion Conference,
Washington D.C., USA
October 6-10, 2013

Michael S. McDonald* and Alec D. Gallimore†
Plasmadynamics and Electric Propulsion Laboratory (PEPL)
University of Michigan, Ann Arbor, MI USA 48109

High-speed imaging at 87,500 frames per second is used to characterize visible spoke and breathing mode oscillations in the H6 Hall thruster across a set of 25 operating conditions forming parameter sweeps in magnetic field strength $|B|$ and discharge voltage V_D at fixed mass flow rate. The study includes three sweeps, all at 10 mg/s anode flow rate, or about 10 A discharge current. The three sweeps are a range of peak channel magnetic fields from 70-230% of the optimal magnetic field strength at a fixed 300 V discharge voltage, a range of discharge voltages from 105 - 600 V at fixed magnetic field strength, and a range of discharge voltages 105 - 600 V with optimized magnetic field strength to minimize mean discharge current. Fourier analysis of each 1-second video is used to reduce each ~10 GB file to a single proposed figure of merit, the dimensionless ratio of the RMS pixel oscillation of the summed spoke modes $m > 0$ to the RMS pixel oscillation of the breathing mode $m = 0$. The parameter study cases show that spoke strength relative to the breathing mode at conditions near to the optimized magnetic field strength to minimize the discharge current. This is due to both changes in spoke strength and discharge current oscillations. Discharge current oscillations are minimized near optimal $|B|$ for a given V_D, with larger increases in oscillation magnitude for a given excursion toward suboptimal $|B|$ vs. superoptimal, and likewise larger increases for given excursions toward suboptimal V_D vs. superoptimal. Spoke velocities are shown to asymptote with increasing mode number in the high 1000 m/s to low 2000 m/s range in the discharge. Bandpass filtering of video pixel intensities at spoke frequencies shows evidence of multiple coexisting spokes, with occasional tradeoffs between dominant modes in the discharge. Statistical analysis suggests that while large 1-second videos with ~10 GB file sizes were acquired here, as little as 10-30 ms videos may be permissible to compute spoke/breathing mode strength ratios with 5-10% error. Finally, to promote the wider application of high-speed imaging as a Hall thruster diagnostics, the MATLAB codes used for high speed analysis in this and previous works are now available as part of an open source integrated toolkit.

I. Introduction

In a trend discussed in more detail previously,[1] the increasing availability of spacecraft solar power on orbit has driven the development of ever higher power Hall thrusters, most recently the triple channel X3 nested Hall thruster with design power level in excess of 100 kW whose first firing is reported at this conference.[2] As higher power thrusters with higher mass flow rates come online, they tax existing ground facilities and incur higher testing and development costs. This trend is exacerbated by poor understanding of electron transport physics, requiring empirical inputs to calibrate accurate thruster models and driving heavily experimental testing regimens to validate new thruster designs. This poor understanding of the means of electron passage across the strong thruster magnetic fields motivates basic research into electron transport mechanisms.

One of the most promising explanations for unexplained electron transport in Hall thrusters in recent years has been the (re-)discovery of low-frequency rotating spokes in numerous Hall thruster discharges.[3–9] Owing to the harsh

*Currently a Karle Postdoctoral Fellow, Naval Center for Space Technology, Naval Research Laboratory, Washington D.C. This work was performed while a postdoctoral researcher at the University of Michigan. msmcdon@umich.edu.

†Arthur F. Thurnau Professor, Department of Aerospace Engineering. Director of the Plasmadynamics and Electric Propulsion Laboratory. alec.gallimore@umich.edu.

plasma environment in thruster discharge channels, whose direct interrogation require either perturbative fixed probes near the discharge channel walls or complicated experimental setups involving high speed motion stages and reciprocating probes of refractory metal and ceramic construction, high-speed imaging has become an attractive nonintrusive alternative to direct probing to detect and characterize rotating spoke propagation frequency and dominant mode structures (i.e., number of spokes simultaneously present). Video data are useful for identifying plasma potential and density oscillations in such probe measurements with visible spoke frequencies, linking local plasma measurements with a global picture of plasma behavior. In addition, it may eventually be possible to calibrate the nonintrusive video diagnostic to relate pixel values to plasma properties.

Analytical theories for spoke formation and propagation such as the recent work by Escobar[10–12] and modeling efforts such as the axial-azimuthal particle-in-cell (PIC) models first developed by Fernandez[13] and recently extended by Garrigues[14] are driven by an effort to account for spoke-induced azimuthal electric fields coupling with applied radial magnetic fields to generate cross-field electron transport. This work extends previous efforts to put quantitative high speed analysis on a firm footing by developing more rigorous means for characterizing spoke velocity, amplitude, and "strength" from high speed video, and applies those techniques to a parameter study of magnetic field strength and discharge voltage in the H6 Hall thruster. The intent is that a comprehensive set of measured spoke modes and velocities and the corresponding discharge conditions will contribute to the development and validation of theories of spoke formation, propagation and effects on cross-field electron transport. Comparison with breathing mode behavior is intended to shed light on the interaction between the two phenomena.

Section II of this paper briefly addresses distinctions between the current study and a previous, similar parameter study.[4] Section III describes the experimental setup and methods, especially the quantitative techniques used for video analysis in this paper, most of which are included in a recently released open-source MATLAB analysis toolkit for Hall thruster video.[15] This section includes a proposed dimensionless ratio of spoke strength to breathing mode strength, relating the level of pixel oscillation observed in spokes to the usually larger breathing mode pixel oscillation. Section IV presents the experimental results from the 25-condition parameter study. Two appendices include full discrete Fourier transforms for all 25 parameter study operating conditions, and a discussion of data management for large multi-gigabyte data files, with statistical analysis to support the acquisition of shorter length videos of 10-30 ms under certain conditions.

II. Relation to Previous Parameter Study

The parameter study that forms the bulk of the experimental results in this paper was inspired by an earlier similar effort, also in the H6 thruster. Several factors motivated an improved version of that earlier study, most notably the 27 kHz limit previously placed on image acquisition due to a less capable camera. With a Nyquist frequency of only 13.5 kHz, most of the dominant breathing mode peaks and many of the higher spoke modes were too fast to be identified. The present study uses an upgraded camera acquiring images at 87.5 kHz, more than sufficient to capture all of the breathing mode oscillations and weak, fast spoke modes up to $m = 7$ and beyond.

A second shortcoming of the previous study was that spoke frequency and amplitude identification was subjective and not repeatable, since it was based on manual best guesses from noisy Fourier spectra. The present effort is automated and repeatable, using an initial guess for peak frequency to seed a functional fit to the power spectral density peaks (Section 4), returning a peak frequency, amplitude, and full-width at half-maximum. Automation has also improved the identification of the thruster discharge channel in an image (Section 1), again increasing comparability across multiple operating conditions.

Third, the previous study attempted to draw conclusions about spoke strength and stability, but failed to develop satisfactory metrics for either quantity. In this work stability is still addressed only qualitatively (see Section E), but the repeatable identification of spectral density peaks by automated fits as well as a new proposed scalar metric for spoke strength vs. the breathing mode allow more quantitative discussions of spoke strength. Taken together, these factors allow a more rigorous review of the earlier conclusions (see Section B), and an extension of the results to demonstrate a clear inverse relationship between breathing mode discharge current amplitude and visible spoke mode strength.

III. Experimental Setup and Methods

A. Vacuum Facility

All videos were taken in the Large Vacuum Test Facility at PEPL. The LVTF is a 9 m long x 6 m diameter cylindrical stainless steel-clad chamber maintained at vacuum by seven CVI TM-1200 re-entrant cryopumps with LN2 baffles and a nominal pumping speed of 500,000 L/s on air (240,000 L/s on xenon). LVTF achieves a base pressure in the low 10^{-7} to high 10^{-8} Torr range and during all videos of thruster operation chamber pressure was below 2×10^{-5} Torr, corrected for xenon.

B. Hall Thruster

The H6 is a 6 kW-class laboratory model Hall thruster with a nominal operating condition at 300 V and 20 mg/s xenon anode flow rate (approximately 20 A discharge current) with a 7% cathode flow fraction. All images in this paper show the H6. It uses an internal cathode mounted coaxially with the the thruster, visible as a bright central dot in Figure 2. The magnetic circuit consists of independent inner and outer magnet coils and an auxiliary trim coil, which is not used here. For the operating cases presented here it is operated with a fixed ratio of currents to the inner and outer magnet coils to maintain an approximately symmetric magnetic field shape across discharge channel centerline. At nominal operation the H6 produces approximately 400 mN of thrust at a specific impulse of about 1900 s. It is notable for its high total efficiency, 60% at nominal operation and 70% at 800 V, 6-kW operation.

For this parameter study the anode mass flow rate was fixed at 10 mg/s xenon, half the design level, with the usual 7% cathode flow fraction. Three paths through the $B - V_D$ parameter space were taken, each centered around a discharge voltage of 300 V and a peak channel magnetic field strength B_{max} optimized to minimize mean discharge current. Values of B_{max} normalized relative to the optimal level that minimized mean discharge current at 300 V are reported. The first path swept B_{max} from 70%-230% of optimal at a fixed 300 V discharge. The second swept V_D from 105 to 600 V with the magnetic field strength fixed at optimal 100% level chosen for 300 V. The third path swept over the 105 - 600 V range but tuned B_{max} to minimize discharge current at each voltage.

C. Camera

All high speed videos were taken using a Photron SA5 FASTCAM with a Nikon ED AF Nikkor 80-200mm lens at or near its maximum aperture f/2.8. A 256x256 pixel resolution was chosen to enable sub-millimeter spatial resolution per pixel of the thruster channel. The 1:1 aspect ratio (square image) captures the entire discharge channel to make unambiguous identification of rotating instabilities. An 87,500 Hz framerate was chosen to place the Hall thruster breathing mode well below the framerate Nyquist frequency. The high-speed camera views the thruster axially through a quartz viewport with an interior sacrificial glass plate cover from approximately 6.5 meters downstream.

In general the camera's raw pixel output does not linearly map to visible light intensity. Non-linearity of the bit depth of the camera sensor causes the pixel output to asymptote and saturate at high incident fluxes. This can be accounted for by calibration if necessary. However, for the particular cases presented here, the high frame rates used keep the light intensity reaching the camera well inside the linear regime. One exception is the cathode, which generally saturates the image. However, the cathode portion of the frame is not used for analysis and does not affect the results presented here.

Visible light detected by the high-speed camera is expected to be emitted from xenon neutrals and ions. For a xenon Hall thruster, the strongest ion emission lines are 484.4 nm, 529.2 nm, and 541.9 nm, while the strongest neutral lines are 823.2 nm and 828.0 nm.[16] However, high-speed imaging through 10 nm wide bandpass filters centered at 540 and 830 nm produced much better signal with the 540 nm filter, even though the neutral emission lines near 830 nm are significantly stronger. Nevertheless, even with the 540 nm filter, framerates above 10-20 kHz captured too little light per exposure to be useful with the Nikkor f/2.8 lens. Thus, in this paper the full spectrum of visible light is captured with the high speed camera, most but not all of which is due to excited ion emission, while due to some combination of lower transmission of lens coatings and lower camera CMOS quantum efficiency in the near-IR wavelengths most neutral emission is not captured.

D. High Speed Video Analysis

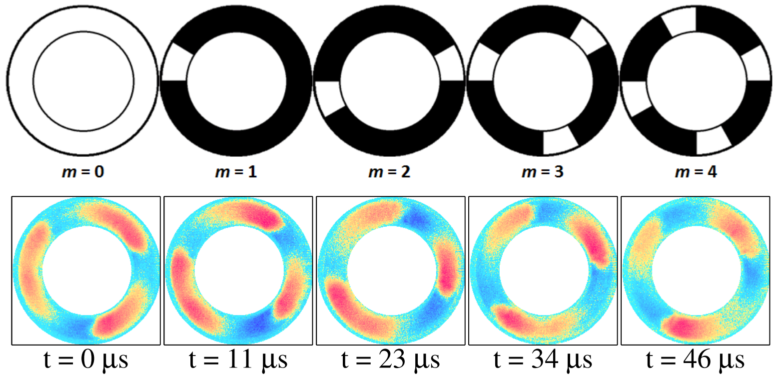

Figure 1. Top, physical meanings of the various spoke modes. White indicates luminous spokes propagating through an otherwise dark background. The mode number m indicates the number of spokes simultaneously present. For $m \geq 1$, the spokes propagate azimuthally in the $E \times B$ direction. For $m = 0$, the entire channel flashes in unison (the breathing mode). Bottom, a false-color image sequence from the H6 Hall thruster operating at 600 V, 10 mg/s, showing a $m = 3$ with warmer colors indicating brighter than average pixel intensity, and cooler colors for dimmer pixels.

Some of the algorithms used for high speed video analysis here have previously been discussed, including definitions of spoke mode structures (m = 1, 2, 3...) and the generation of false-color enhanced images like in Figure 1.[3,17] Qualitative spoke visualization techniques will not be further addressed here, but improvements to the quantitative Fourier analysis of videos motivate their review. These algorithms have also recently been implemented into a largely automated MATLAB analysis toolkit for the import, Fourier analysis, and mode identification of Hall thruster video. The toolkit has been released as an open-source project for collaborative input and questions may be directed to the first author.[15]

1. Automated Thruster Channel Identification

The previous discussion illustrated qualitative differences between thruster operating conditions with strong breathing mode oscillations and strong spoke mode oscillations. This section applies Fourier analysis to the videos, identifies the oscillatory modes in the Fourier power spectrum, and presents metrics to quantitatively compare their strengths.

For reproducible results an automated procedure is used to crop the thruster image and focus on the discharge channel. First, a mean image computed over a full video is used to generate a histogram of all pixel values (Figure 2). The center of gravity of these pixel values is used to compute a threshold below which pixels are discarded for use in the circle fit. This eliminates the vast majority of dim pixels outside the bright thruster channel. Once bright pixels have been identified, methods by both Kasa and Taubin have been implemented to fit a circle to the pixels.[18,19] Only the x-y position of the pixels is considered; the fit is unweighted by pixel value.

Kasa's least-squares fit is fast and relatively simple to implement, but is inaccurate when the whole channel is not captured in an image (a common experimental reality) and underestimates the correct circle radius while shifting the circle center toward the imaged arc section. Taubin's singular value decomposition (SVD) method is preferred for its more robust treatment of partial images, and per-

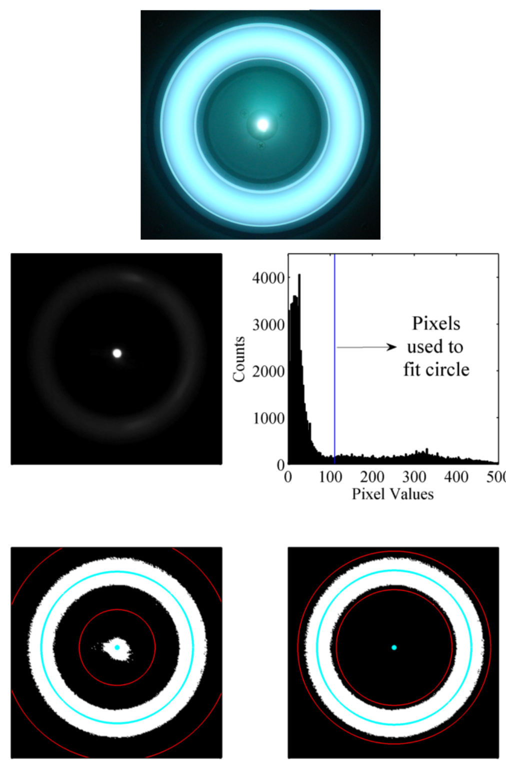

Figure 2. Automated thruster circle fitting process. Above, a color still image of the H6 thruster. Middle left, a raw mean video image. Middle right, the "center of gravity" of a histogram of pixel values is used as a brightness threshold. Lower left, pixels brighter than the threshold are used for an initial circle fit. Pixels <50% or >150% (red lines) of the calculated radius are cropped. Lower right, an iterated fit on the remaining pixels is performed. Only pixels within 75%-125% of the iterated radius are Fourier analyzed.

forms good circle fits down to only a 90-degree capture of the full channel. For more discussion of circle-fitting algorithms, refer to the comprehensive monograph by Chernov.[20]

Once an initial fit is performed based on the pixels above the center of gravity brightness, the fit is refined by cropping any bright pixels found inside 50% or outside 150% of the calculated radius (red lines in lower left image of Figure 2). This effectively removes the bright spots from most internal or external cathodes. The same Taubin SVD fit is performed on the new pixel population, and the Fourier analysis of the next section uses pixels within 75% to 125% of the radius of the iterated fit with outside pixels set to zero (lower right, Figure 2).

2. *Use of Fourier Analysis to Compute Power Spectra*

Large video files motivate analysis in the frequency domain for data reduction to more manageable sizes. Power spectra from discrete Fourier transforms (DFTs) of the video identify rotating spoke modes, propagation velocity and strengths of competing oscillatory modes. The DFT is applied to a dimensionally reduced form of the video dubbed the "spoke surface". All DFTs are calculated using the fast Fourier transform (FFT) algorithm with the built-in '*fft*' or '*fft2*' commands in MATLAB.

Consider a video as a 3D matrix of pixels $p(i, j, k)$. The full 3D DFT of $p(i, j, k)$ is neither practical for display nor terribly informative. Instead, the 3D video is reduced to 2D. To examine rotating instabilities, consider the pixel values p in polar coordinates $p \rightarrow p(r, \theta, k)$. Dividing the 360 degrees of the annular discharge channel into discrete angular bins with N_b pixels in the b^{th} bin and computing average pixel intensities $\bar{p}$ in each bin (see Figure 3) collapses the radial video dimension to produce a set of azimuthal profiles:

$$\bar{p}(\theta_b, k) = \frac{1}{N_b} \sum_{i=1}^{N_b} p_i(r, \theta_b, k)$$

Taken together, these azimuthal profiles form a 2D matrix dubbed the "spoke surface". The spoke surface matrix has columns equal to the number of azimuthal bins and rows equal to the number of video frames. Angled parallel striations in the spoke surface correspond to spoke modes propagating azimuthally with time, while horizontal striations correspond to the breathing mode appearing in unison across the entire channel (see Figure 4, left).

The DFT is complex, but its product with its complex conjugate gives a real quantity, the power spectral density (PSD). The DFT, PSD and input signal all have matching dimensions, so a 1-second, 100,000-image, 180-bin spoke surface has a PSD with 100,000 rows for frequencies from 0 - 99,999 Hz and 180 columns for sinusoids with wavelengths from 2π / (0 - 179) radians. The 0 Hz frequency is for DC signals, while the $2\pi/0$ "infinite" wavelength is for unified oscillations of pixel brightness across the entire 2π of the discharge channel. The DFT and PSD columns correspond to the modes m = 0, 1, 2, shown above in Figure 1 and are defined as

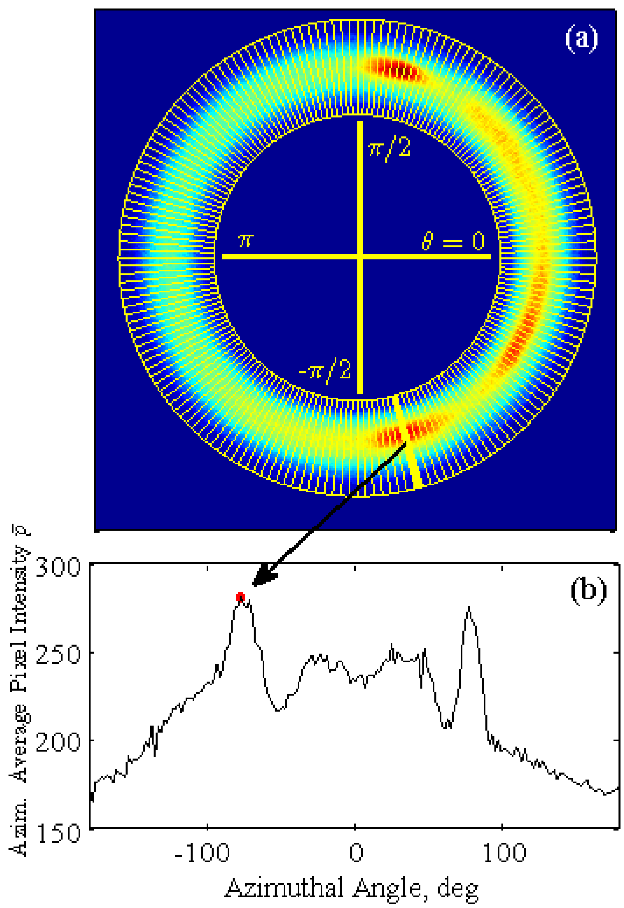

Figure 3. A 2D Cartesian video frame is a) converted to polar coordinates and azimuthally binned, and (b) reduced to 1D by computing an average azimuthal pixel intensity $\bar{p}$. The collection of these 1D profiles of $\bar{p}$ forms the 2D spoke surface.

$$m \equiv k_\theta R = \frac{2\pi R}{\lambda}$$

where k is the wavenumber and R is the channel radius.

The PSD matrix is doubly symmetric, since signals propagating clockwise at 1/4 revolution per frame are indistinguishable from those propagating counterclockwise at 3/4 revolution per frame. A small section of the unique quadrant of the PSD is displayed in the middle of Figure 4; the upper half of the frequency axis is truncated at the Nyquist frequency of the framerate, and the amplitudes of modes with large m are negligible. The DFT and PSD are discrete matrices, but the fine frequency resolution gives the PSD the appearance of a continuum in the figure.

In the final PSD representation at right in Figure 4, the non-negligible columns are broken out, smoothed of noise, and plotted individually. For smoothing, the power spectrum values in a given frequency range are assumed to consist of a normal distribution of amplitudes. Within each of these ranges a mean amplitude and standard deviation σ are calculated, and both the mean and upper and lower bounds of a 95% confidence interval ($\pm 3\sigma$) are plotted, with the mean in bold and the confidence interval spanned by lighter lines for each oscillatory mode. The exact width of the frequency range used for filtering varies depending on the dataset, but a minimum of 50 elements per range and 50 filtering ranges per spectrum are enforced. For a 1 s video with 1 Hz resolution this reduces resolution to 50 Hz. By inspection in Figure 4 this strikes a reasonable balance between smoothness and frequency resolution.

The units of the PSD are traditionally amplitude^2 / Hz, allowing the area under the curves to be interpreted as a total power. However, this form can be confusing because the peak amplitudes do not linearly relate to the amplitude of the average pixel intensity $\bar{p}$ oscillations. This is addressed later, in Section 5. First, the physical meaning of the various peaks is addressed.

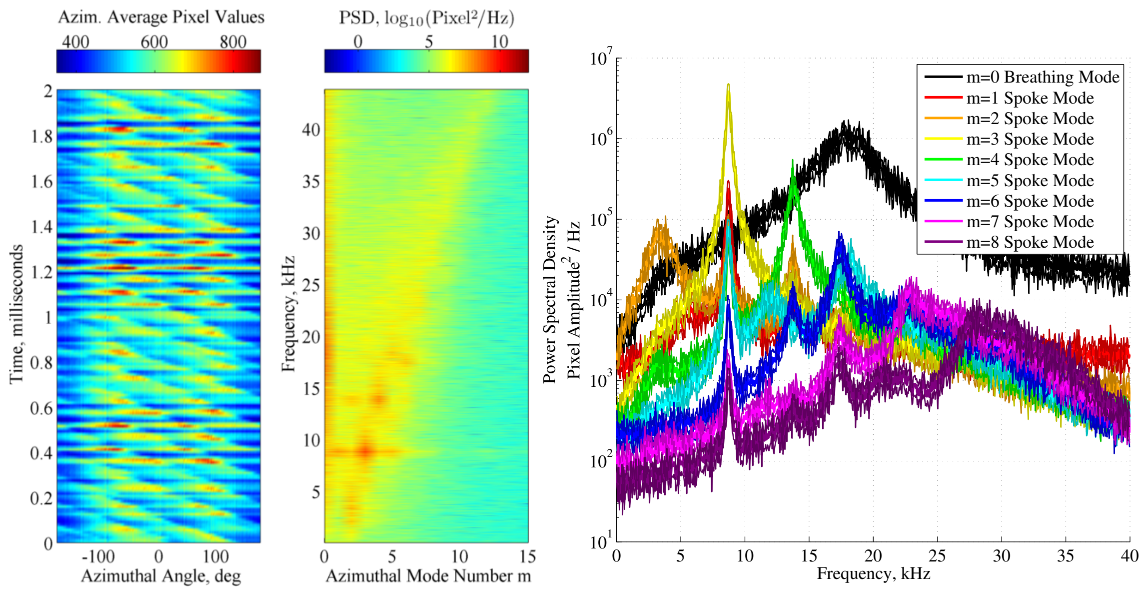

Figure 4. The spoke surface (left) is a 2D matrix composed of the average pixel intensities for each frame in a video. The power spectral density or PSD (middle) shows peaks corresponding to standing and propagating waves. The diagonal pattern in the PSD empirically illustrates the dispersion relation for propagating spokes in the Hall thruster. The columns of the PSD may be broken out for easier representation (right). The rightmost figure is here referred to as the 2D DFT of a video, though strictly speaking it is a set of 1D representations.

3. Interpretation of the PSD

The relative amplitudes of the different modes in the PSD indicate which oscillation types are most strongly visible to the camera. Typically one mode is strongest, like the threefold $m = 3$ spoke mode in Figure 4, but there are a number of harmonics and other artifacts for many modes. PSDs for all 25 operating conditions examined in this paper are included in the Appendix and further illustrate many of these features. Consider the two cases in Figure 5. The left case has strong $m = 2$ and $m = 3$ modes at 3 and 8 kHz, respectively, and the $m = 3$ mode peak exceeds the $m = 0$ breathing mode. In the right case the $m = 2$ and $m = 3$ modes are also dominant, but with several other peaks besides the main ones.

Most of these peaks appear to be nonphysical artifacts of the Fourier decomposition. When the average azimuthal bin pixel intensity (Figure 3) has sharp edges, they cannot be accurately represented by a single frequency component and will require more frequencies to reconstruct the shape. For example, the $m = 3$ mode in the false color image from Figure 1 has a sawtooth-like azimuthal profile due to its sharp edges, which may show up as harmonics at $m = 6$,

$m = 9$ and beyond to reproduce it. Harmonics are easy to spot because they have integer multiples of frequency and mode number, corresponding to the same propagation velocity (Equation 1). For example, the right case in Figure 5 has $m = 4$ and $m = 6$ peaks near 6.6 and 9.9 kHz that are second and third harmonics of the $m = 2$ mode at 3.3 kHz. Another probable artifact is what appears to be a beat mode, the $m = 5$ mode at 11 kHz. Compared to the $m = 2$ and $m = 3$ modes, it has a mode number equal to their sum and a linear velocity (Eqn. 1) equal to their average.

A trickier issue is the multiple smaller peaks seen in other modes at the same frequency as a dominant mode. Clear examples are below the $m = 3$ mode in both left and right PSDs in Figure 5. Previously these were described as "turbulent smearing" of the dominant mode because of the tendency of the dominant spoke structure to sometimes briefly gain or lose a spoke without significantly changing speed.[4,17] The effect is noticeable only for large amplitude spoke or breathing modes, but amplitude alone is not the cause – simulating a spoke surface with breathing and spoke modes does not show this behavior regardless of amplitude, even in the presence of large amounts of random noise. Further support of this being an artifact is the absence of alternate mode structures in the binwise-filtered spoke surfaces discussed in Section E.

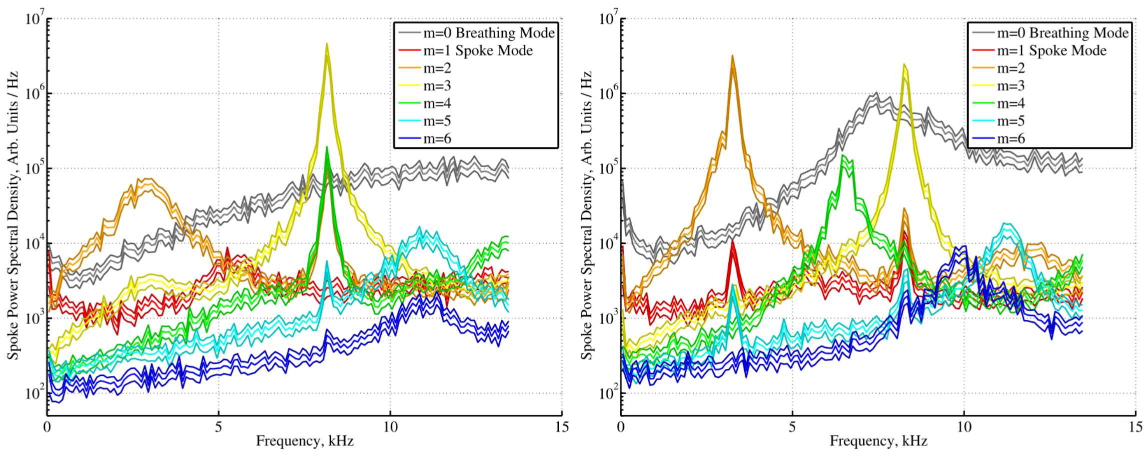

Figure 5. Example DFTs illustrating several subtle features of mode analysis. At left the dominant $m = 3$ mode at 8 kHz has spurious $m = 2$ and $m = 4$ peaks at the same frequency. At right the $m = 2$ mode has higher harmonics $m = 4$ and $m = 6$, as well as a $m = 5$ beat mode.

4. *Calculation of Spoke Velocity*

Given a spoke frequency f_m, the linear velocity v_m of spoke passage around the discharge channel for a spoke mode m is given for all $m \geq 1$ by

$$v_m = \frac{2\pi R f_m}{m} \tag{1}$$

For the H6 Hall thruster a $m = 1$ spoke mode with $f_1 = 1$ kHz travels at an approximate velocity $v_1 = 500$ m/s. The $^1/_m$ term in the linear velocity equation is because the 2D PSD gives a local frequency at a fixed azimuthal location – if m spokes are present, the local frequency is boosted by a factor of m compared to the global rotation frequency of any single spoke. Thus, a $m = 2$ spoke mode with $f_2 = 1$ kHz in the DFT or PSD only has a linear spoke velocity of 250 m/s, compared to 500 m/s for the $m = 1$ mode with the same frequency. Since the $m = 2$ mode is composed of two spokes, each propagating at 500 Hz but spaced 180 degrees apart, a local observer in the discharge channel observes recurring spokes at 1 kHz. An $m = 1$ spoke mode with a single spoke must travel twice as fast to recur at the same frequency to the local observer. Plasma probes are just such local observers, and unlike video cannot distinguish between modes with different global frequencies that manifest at the same local frequency without a second nearby probe for signal cross-correlation.

Repeatable manual identification of a single frequency peak in a noisy PSD plot is difficult, even for smoothed PSDs, so a fitting procedure is used to locate the peak frequency f_m. By visual inspection, the PSDs resemble the resonance peak of a forced harmonic oscillator with damping. For a strong resonance, the exact harmonic oscillator solution may be approximated near the peak by the Lorentzian distribution:[21]

$$A(f) = \frac{A_0}{1 + \frac{(f-f_0)^2}{\gamma^2}} \tag{2}$$

where the curve peaks at frequency f_0 with amplitude A_0 and full-width at half-maximum (FWHM) γ. While the exact physical mechanism driving the spoke oscillations is not understood, the fits produced are compelling (Figure 6) and provide a semi-automated mechanism for identifying peaks in noisy DFTs. One shortcoming is that the nonlinear least-squares routine used to compute the fits requires good initial guesses.

The oscillator amplitude A_0 is a fair estimate of mode strength between modes within a single PSD, but its absolute level depends on several experimental details, discussed in the next section along with a more reliable way to gauge spoke strength.

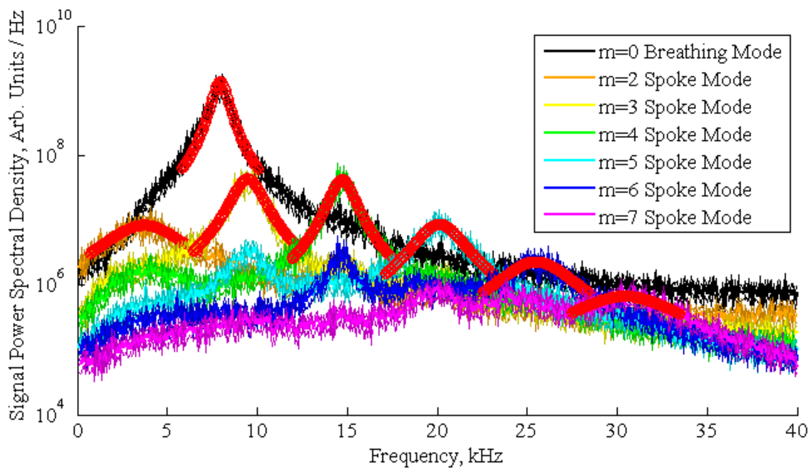

Figure 6. Lorentzian fits to video PSD used for frequency peak identification

5. Scalar Metric for Spoke Strength

Fourier analysis is well-suited to reducing a large, 1-10 GB video to a single plot. However, comparisons across several PSDs are still relatively qualitative. The peak values in the PSD depend physically on camera CCD quantum sensitivity, lens aperture size (e.g., f-stop), shutter speed or exposure time, thruster, and operating condition, and in postprocessing are sensitive to the degree of cropping of the discharge channel, number of bins and level of smoothing applied. Since these factors are constant across all videos in the parameter study, they may be used directly as a measure of spoke strength for comparison within the study cases. However, a more general metric insensitive to these factors is desirable for comparison across different thrusters, cameras, and facilities processed by different investigators. This section describes reduction of the PSD to such a single scalar metric of spoke strength to facilitate wider data comparison.

Recall that a 1D DFT of a discrete 1D signal x_n of length N gives a finite series of N sinusoidal basis functions with different amplitudes. These components represent $N-1$ oscillations in time at different temporal frequencies as well as one constant or zero-frequency component. The 2D spoke surface PSD shows pixel oscillations with both spatial and temporal frequencies, allowing for four distinct types of signal. The first is the trivial mean DC component, unvarying in both time and space. The second type is spatially constant but varying in time – the $m = 0$ mode with its overall dimming and brightening. The third is an angularly varying signal constant in time, for example if one azimuthal location is consistently brighter throughout a video as seen on the mean image from the full video. The fourth and final type is a wave, such as the rotating spokes with $m > 0$.

Parseval's theorem in Fourier analysis states that, for the DFT X_k of the signal x_n above, the root-mean-square (RMS) of the original time-domain signal and its DFT are equal:

$$\sum_{n=1}^{N} |x_n|^2 = \frac{1}{N} \sum_{k=1}^{N} |X_k|^2$$

Physically, Parseval's theorem reflects that the energy content of a signal is independent of its representation in time or frequency space. In the case of the 2D spoke surface, the analogous expression is

$$\sum_{m=1}^{M} \sum_{n=1}^{N} |x_{mn}|^2 = \frac{1}{MN} \sum_{j=1}^{M} \sum_{k=1}^{N} \left|X_{jk}\right|^2$$

Note that the $\frac{1}{MN}\left|X_{jk}\right|^2$ are the values plotted in the PSDs in Figures 4 and 5. By selectively summing over appropriate regions of a spoke surface PSD, the RMS values of each of the four types of oscillations may be obtained.

$$RMS = \frac{1}{MN} \begin{cases} |X_{11}| & \text{Uniform Mean Image} \\ \sqrt{\sum_{k=2}^{N} |X_{1k}|^2} & \text{Nonuniform Mean Image} \\ \sqrt{\sum_{j=2}^{M} \left|X_{j1}\right|^2} & \text{Breathing Mode } (m = 0) \\ \sqrt{\sum_{j=2}^{M} \sum_{k=2}^{N} \left|X_{jk}\right|^2} & \text{Spoke Modes } (m > 0) \end{cases} \tag{3}$$

The DC component given by the corner element in the first row and first column of $|X|$represents the mean value of the average pixel intensity in each azimuthal bin of the spoke surface (for a DC signal, RMS = amplitude). Since each bin's value was an average over the pixels within that bin, this is just the average pixel value over the entire discharge channel. The RMS of the static azimuthal variation of pixel values (the nonuniform mean image) is given by the root of the sum of the rest of the elements in the first row, divided by MN. The pixel RMS of the breathing mode $m = 0$ oscillation is given by the root-sum of the rest of the elements in the first column divided by MN, while the combined pixel RMS for all modes $m > 0$ may be found with the root sum of the rest of the elements divided by MN. The RMS for all modes can be found in one lump sum because the modes m representing oscillations $sin\,(m\theta - \omega_m t)$are orthogonal, thus their RMS values add in quadrature. To compute the RMS values for individual modes, note that for all columns except $m = 0$ and $m = N/2$ the mode's energy is split between the symmetric halves, so the RMS pixel oscillation for these modes is $\sqrt{2}$ times the root-sum of the appropriate column. Also, the inter-modal "bleeding" or "smearing" artifacts can throw off these RMS values.

Given these definitions, we propose the ratio of the spoke mode $m > 0$ RMS pixel oscillation to the $m = 0$ RMS pixel oscillation as a dimensionless figure of merit:

$$\text{Dimensionless Spoke Strength} = \frac{\text{Breathing Mode } (m = 0) \text{ RMS}}{\text{Spoke Modes } (m > 0) \text{ RMS}} = \frac{\sqrt{\sum_{j=2}^{M} \sum_{k=2}^{N} \left|X_{jk}\right|^2}}{\sqrt{\sum_{j=2}^{M} \left|X_{j1}\right|^2}} \tag{4}$$

The benefit of this metric is that most if not all of the situation-dependent factors enumerated above (lens sensitivity, shutter speed, camera sensor, etc.) should cancel out in the ratio, so it should be relatively well-suited for wide comparison. The ratio typically has a value between 0 and 1.

Unlike the ratio, the spoke mode $m > 0$ RMS alone does depend on specific experimental parameters, and it is also sometimes skewed because strong breathing mode oscillations "smear" into the spoke spectra, similar to the "turbulent smearing" between spoke modes discussed briefly in Section 3. Smearing power from one spoke mode to another is not a problem when judging total spoke strength, since all the modes are counted together, but in very strong breathing mode cases it artificially inflates the $m > 0$ RMS pixel oscillation, sometimes dramatically. To compensate for this we removed the smearing by bandstop filtering each bin in the spoke surface at the breathing mode frequency (and occasionally its second harmonic as well) with a narrow bandpass of 1-2 kHz using an 18th order Butterworth digital filter (MATLAB functions '*butter*' and '*filtfilt*'). In Section 9 we will show that the same qualitative trends can be observed using both spoke strength alone and the spoke/breathing mode ratio, making the ratio preferred since it should be more general.

IV. Experimental Results and Discussion

This section presents collected results from a 25-condition parameter study of the effects of magnetic field strength and discharge voltage varied across the majority of the H6 operational range. To conserve xenon, most of the points are acquired at a 10 mg/s flowrate, half the nominal design condition.

The parameter study is made up of three datasets: varied discharge voltage at constant magnetic field (denoted 'V', for voltage), varied magnetic field at constant discharge voltage (denoted 'B', for B-field), and magnetic field optimized to minimize discharge current at a given discharge voltage (denoted 'O', for optimized). The 'B' and 'V' datasets form a cross in parameter space intersecting at the 300 V operating condition. The optimized B-field strength at 300 V was used for all other voltages in the 'V' dataset, and the 'B' dataset consisted of several different magnetic field strengths applied at 300 V. The optimized 'O' dataset follows a complicated path in B-V space, with clear increases of $|B|$ with V_D for $V_D > 300$ V, but little change in $|B|$ for $V_D < 300$ V, such that the optimized 105 V magnetic field strength was actually the same as at 300 V. To preserve thruster stability, at the 105 V condition the cathode heater was supplied with 4 A or about 25 W heating power. At all other conditions the cathode heater and keeper were off.

A. Discharge Current Oscillations

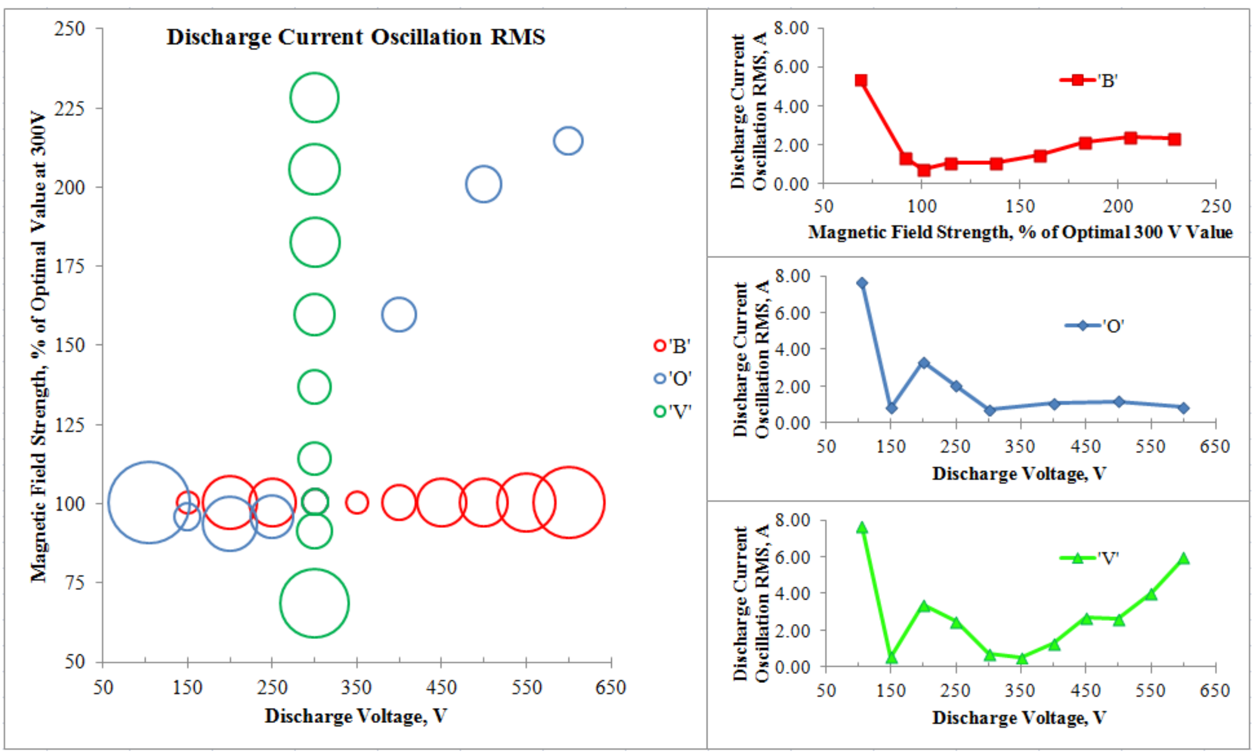

Figure 7. Discharge Current Oscillations

Over the $B - V_D$ parameter space the RMS current oscillation ranges from 0.52 A to 7.62 A, a 15-fold range, while the mean discharge current spans a much more moderate band from 8.6 - 10.8 A. The RMS discharge current oscillation over the parameter space for each of the three sweeps 'B' (magnetic field), 'V' (discharge voltage) and 'O' (optimized B) is shown in Figure 7. The line plots show RMS current oscillations for each sweep individually, while the bubble chart shows the same information for all three sweeps at once, with the bubble area corresponding to the RMS current while the x-y axes show position in the B-V parameter space. Together, the line and bubble plots show the following trends:

1. First, away from the optimized magnetic field strength in V, the ratio of RMS/mean current increases substantially.

2. Second, that behavior is asymmetric, with oscillations becoming much larger with small excursions toward weaker magnetic field (suboptimal) than toward stronger magnetic field (superoptimal). At 300 V and 70% optimal B_{max} the RMS oscillation is 5.4 A A, while at 230% B_{max} the RMS oscillation has only risen to 2.3 A.

3. Third, if one considers the optimized magnetic field settings given by the O dataset as a dividing line between suboptimal and superoptimal magnetic field strength for a given voltage, then the cases at large voltage in the V sweep are in the suboptimal region and also exhibit increased RMS current oscillations compared to the mean level.

Note that the dividing "line" of optimized magnetic field strength at a given discharge voltage denoted by O is not linear (or even monotonic) at low voltage, suggesting different physical mechanisms are at work here than at higher voltages. However, the low voltage V-cases lie slightly to the superoptimal side, so the very similar RMS values are consistent with the observation of gradual changes of RMS current with superoptimal B.

At first glance there also appears to be a trend toward higher oscillation RMS at lower voltages, but the two 150 V conditions are clear outliers to this trend. The tiny variation in optimum magnetic field over a range of nearly 200 V in V_D from 105-300 V is puzzling. The quiescent 150V conditions, bounded on either side at 105 V and 200 V by more oscillatory conditions, are surprising spots of calm in the low voltage region, and will appear out of place in later plots as well.

B. Spoke and Breathing Mode Frequencies, Velocities and Amplitudes

The earlier parameter study[4] reported that higher spoke modes travel faster, and that is confirmed here. It was also previously reported that spoke frequencies asymptotically approach a lower bound with increasing magnetic field strength. The reduction in spoke velocity (and thus frequency) is also supported here, but the existence of an asymptote is not clear. While the $m = 2$ mode appears to level at higher velocities, the higher modes do not.

Reviewing the conclusions of the earlier, similar high-speed imaging spoke parameter study mentioned in Section II and comparing to Figure 8, we find:

1. *Higher spoke modes travel faster.* This is shown to be unambiguously true. In almost all cases, regardless of absolute velocity, the $m = 3$ mode travels faster than $m = 2$, $m = 4$ faster than $m = 3$, and so on. The only exceptions are the 105 V case (shared between the 'O' and 'V' sweeps) and the lowest 'B' case at 70% B_{max}. Examining the 2D DFTs in the Appendix, it is clear that these cases are quite different from the others, with enormously large breathing modes and nothing resembling a spoke peak for any of the modes. Instead, the Lorentzian fits are to broadband bulges with FWHMs ~10 kHz or more.

2. *Spokes in general appear more strongly and stably at higher magnetic field strengths.* This is only true up to a point. There is an optimum magnetic field strength that minimizes the breathing mode and gives larger spoke strengths. Values slightly larger than this optimum have minimal effect, increasing breathing mode amplitude slightly but otherwise maintaining or even increasing spoke strength as well. However, further increases in $|B|$ slowly cause discharge current oscillations to rise while spoke amplitudes basically level out. Decreases in $|B|$ to even slightly suboptimal magnetic field strengths show larger increases in breathing mode oscillations, suggesting the safest spot for quiet operation is in fact slightly above the strength that minimizes mean discharge current.

3. *Higher spoke modes become more dominant at higher magnetic field settings.* While the $m = 4$ mode is slightly stronger near the maximum $|B|$ case, there is not enough data to support the trend. Across the vast majority of cases, the $m = 3$ mode is dominant in the H6, regardless of $|B|$. This is consistent with reports from the X2 dual channel nested Hall thruster where the dominant spoke mode wavelength was 12-17 cm in each channel at both 150 V and 250 V single- and dual-channel operation.[1]

4. *Spoke velocity appears to decrease slightly and/or asymptote at higher magnetic fields.* Confirmed, the velocities of all spoke modes decreased with increasing magnetic field here. However, a velocity asymptote with increasing $|B|$ is unconfirmed. The $m = 2$ mode leveled out to a relatively constant velocity by the highest magnetic field settings, but the higher spoke modes do not appear to be leveling.

A feature not previously noted is that spoke velocity appears to asymptote to a limiting velocity with increasing mode number. This is clearest in the cases with modes identified all the way to $m = 7$, where the velocities of the $m = 5$, 6 and 7 modes all lie nearly on top of one another.

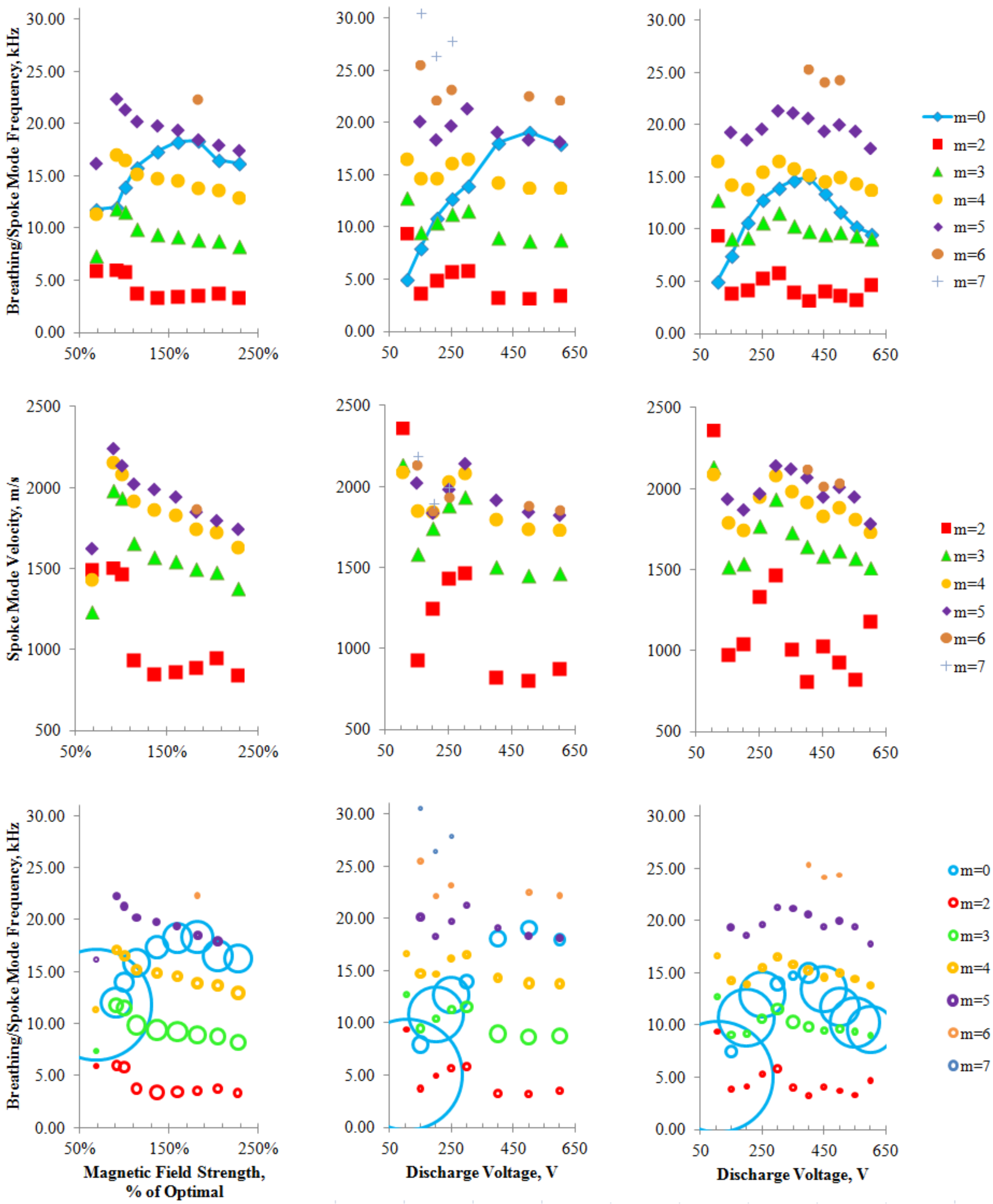

Figure 8. Summarized Results of 2D Video DFTs. Columns from left to right: 'B' parameter sweep, 'O' parameter sweep, 'V' parameter sweep. Rows from top to bottom: mode frequency, mode velocity (spoke modes only), peak Lorentzian mode amplitude. The bottom chart is a bubble chart, duplicating the x-y information from the frequency chart and showing mode amplitude as proportional to the area of the bubbles.

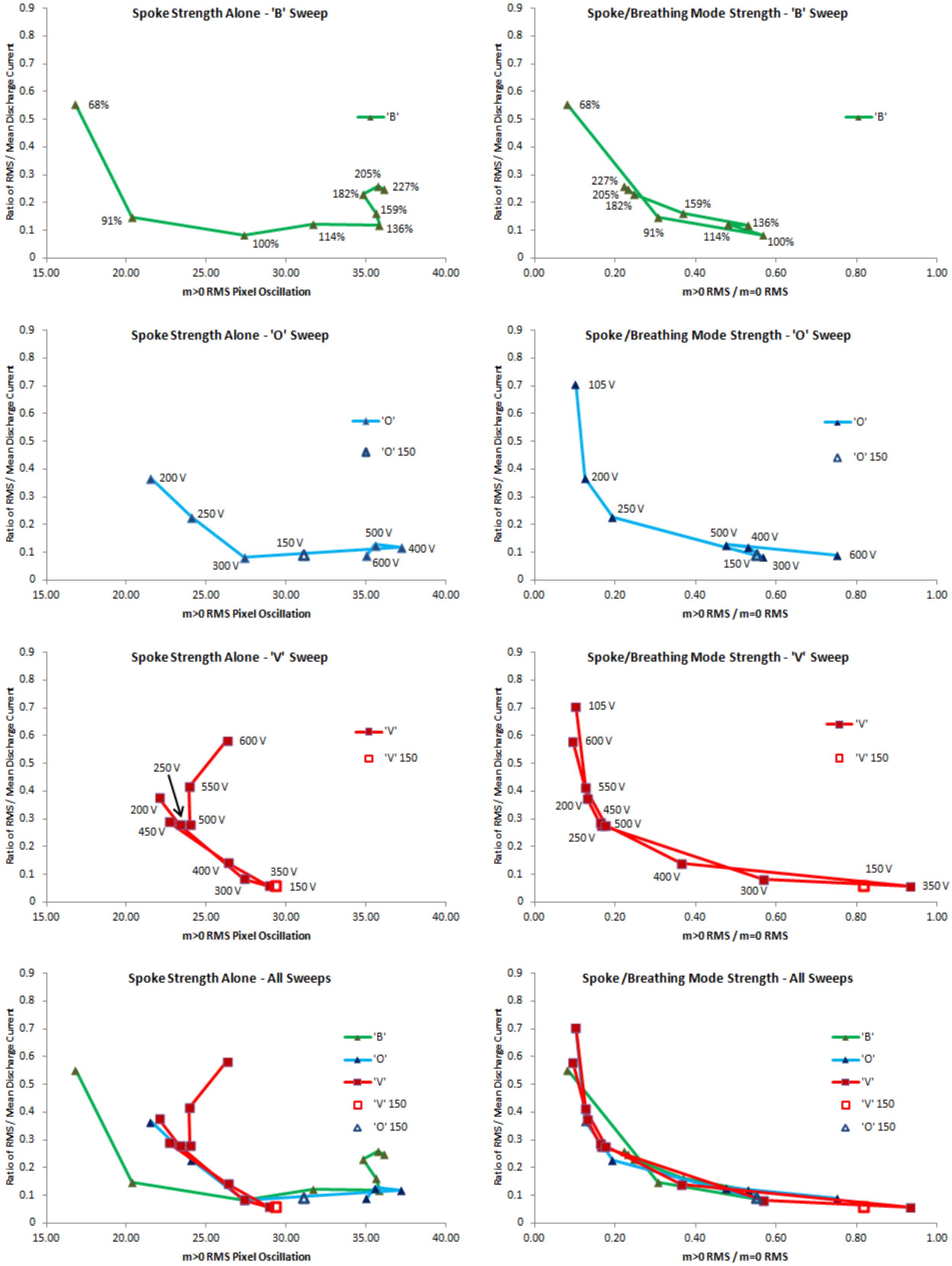

Figure 9. Spoke strengths using independent $m > 0$ RMS spoke strength (left column) and dimensionless ratio of $m > 0/m = 0$ (right column). 'B', 'O', and 'V' parameter sweeps are shown in the first three rows, and combined in the last row. The bottom right chart shows the so-called "main sequence".

C. Relationship Between Breathing and Spoke Mode Strengths

This section examines spoke and breathing mode strengths together across the parameter study videos. Figure 9 plots the RMS/mean discharge current versus the video-calculated RMS pixel oscillations (see Section 5) for the 25 operating conditions in two columns, one for each of the spoke and spoke/breath ratio measures, and four rows, one each for the 'B', 'O' and 'V' sweeps separately as well as a row for all three collected together.

The left column shows the spoke-only strength. In the 'B' sweep, the RMS/mean current oscillation increases for either suboptimal or superoptimal $|B|$, but much faster in the suboptimal direction, just as previously noted in Figure 7. It also shows that the RMS spoke pixel oscillation starts out very weak with the suboptimal $|B|$ cases, increasing rapidly in strength up to and past the optimal magnetic field strength before plateauing from 136%-227% $|B|$ as the discharge current oscillations slowly rise again. The 'O' sweep starts in a similar place as the 'B' sweep, with large discharge current oscillations and relatively small spoke strength, before driving down into the lower right corner of the chart with strong spokes and a weak breathing mode and staying there as voltage increases. The 105 V case is not shown because the enormous breathing mode and its several harmonics in the PSD could not be satisfactorily filtered. The 'V' sweep again starts in a region with relatively large breathing mode strength and weak spoke strength, drives down into the lower right region with low current oscillations and strong spokes as it hits 300-400 V, but then retreats back to where it started in the strong current oscillation / weak spokes regime.

In both the 'O' and 'V' cases, the 150 V case is a clear outlier and is shown separately for emphasis. For reasons that are not at all clear these conditions exhibited much lower current oscillations and stronger spokes than would normally have been expected at that discharge voltage. It is not surprising that the two 150 V outliers are close together; their magnetic field strengths differ by <5%.

The right column shows the dimensionless spoke/breathing mode RMS ratio defined in Eqn. 4. The same trends are visible in the 'B' sweep as before, but the sweep traces out nearly the same path on its return with increasing superoptimal $|B|$ as it did on its descent with suboptimal $|B|$. This is because the increase and plateau in independent spoke strength with superoptimal $|B|$ is associated with a rise in discharge current, so the dimensionless spoke strength's $m > 0/m = 0$ RMS ratio drops. The 'O' sweep looks basically the same, driving into the lower right corner of the chart with low discharge current oscillations and high spoke strengths. Finally, the 'V' sweep shows a very similar behavior to the 'B' sweep, diving into the lower right as V_D approaches optimal and then receding back into the upper right with increasing superoptimal V_D.

The bottom row shows an interesting collapse of the three parameter sweeps into a single "main sequence" of conditions showing that spokes are visibly strongest relative to the breathing mode near conditions where the magnetic field strength is optimized to minimize the mean discharge current. Among such optimized cases, higher discharge voltage conditions have larger spoke strengths relative to the breathing mode. The 1/x hyperbola shape of the curve is to be expected because the $m = 0$ RMS pixel oscillation is close to linearly related to the RMS discharge current oscillation (see Figure 10).

Since the mean discharge current varies only slightly, the spoke/breathing mode ratio essentially has the discharge current RMS/mean built into its numerator, causing the 1/x shape of the curve in Figure 9. However, the general trend of maximized spoke strength relative to breathing mode near optimized magnet conditions is still valid, and the ratio combats most of the skewing in spoke pixel RMS calculation caused by smearing from strong breathing modes.

Taken together, the curves show that spoke strength increases up to and past optimal $|B|$ until they saturate, at which point discharge current oscillations or breathing mode strengths slowly increase again. For optimized magnetic field strengths the spoke strength saturates at higher voltage but the discharge current oscillations drop with increasing voltage and do not appreciably rise again. Finally, at fixed $|B|$ the effect of varied V_D is much stronger on V_D than on spoke strength. The spoke strength increases slightly approaching the V_D where $|B|$ was optimized, following basically the same path from 100-300 V as the 'O' sweep did since the conditions are quite similar, and once V_D is too large for a given $|B|$ the same rapid increase in discharge current oscillation occurs as when $|B|$ was too small for a given V_D.

Further work is needed to check whether the overlapping of all three traces in the bottom right of Figure 9 is a coincidence due to the small variation in spoke pixel RMS compared to the larger variations in breathing mode strength, or if it is a more general pattern that other thrusters will fall on as well. If it is a general pattern, knowing where a thruster operating condition falls on this sequence might provide predictive power for how to improve thruster operation by reducing discharge current oscillations.

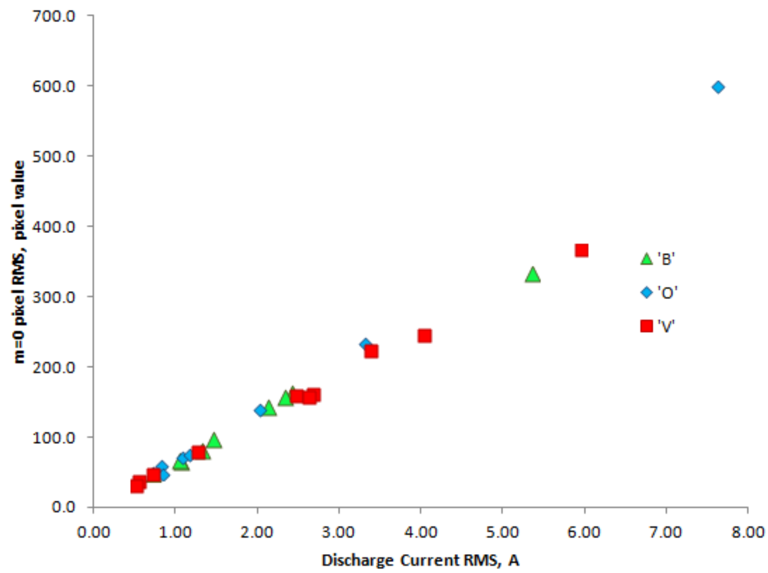

Figure 10. Linear relationship between discharge current RMS in amperes and m = 0 pixel RMS across parameter study

D. Relation Between Spoke Strength and Efficiency

While not reported in detail here, thrust stand measurements and efficiency calculations were made at each parameter study operating condition. While one might expect that the highest efficiency cases were in the lower right corner of the charts in Figure 9, this was not always the case. In the 'B' sweep efficiency ranged from a low of 56% at minimum $|B|$ to reach 62% efficiency at 137% of optimum $|B|$ before dropping to 58% at max field strength. The 'O' sweep rose from a low of 27% at the 105 V case to 61% at 300 V and 70% at 600 V (note that all efficiencies are anode efficiencies only). The 'V' sweep rose from 43% at 150 V to plateau at 62-64% from 300-600 V.

Thus, both extremes of the 'B' sweep (both sub- and superoptimal) were in the upper 50% range, while the 105 V condition had a paltry 27% efficiency and was in the same region of the plot. Moreover, the 150 V conditions had efficiencies in the low-mid 40% range in spite of sitting near the bottom right of the plot.

It seems reasonable to say that a high spoke/breathing mode ratio in general may be associated with good efficiency, but with the significant caveat that this is neither necessary nor sufficient to ensure good efficiency. Efficient operating conditions at high V_D exist with low spoke/breath ratios, and there are certain low-voltage, relatively low efficiency conditions with strong spoke/breath ratios too. The more interesting application may be in promoting spoke strength to determine if this can reduce breathing mode discharge current oscillations. This is oddly opposite to the trend observed in cylindrical Hall thrusters, where suppressing spokes leads to reduced discharge current oscillations, and suggests different physics may be at work in annular thrusters.[9]

E. Demonstration of Simultaneously Coexisting Spoke Modes and Mode-Hopping

Previous investigations have been unable to tell whether multiple spoke modes coexist simultaneously or else trade off rapidly in a thruster discharge. The PSD is not well-suited to determining this sort of temporal stability (see the discussion of Fourier analysis, temporal resolution, and wavelets in our companion paper[22]), so while in video the spokes often appear to trade off or mode-hop, there are not yet tools to quantitatively measure mode stability. However, using the spoke frequencies and FWHMs identified by the Lorentzian fits, it is possible to band-pass filter each azimuthal bin in the spoke surface at the various spoke frequencies to qualitatively judge spoke mode coexistence.

Figures 11 and 12 show binwise-filtered spoke surfaces for each of the 400 V and 600 V conditions in the 'O' optimized B-field sweep from the parameter study. For reference, both their 2D PSDs with fitted Lorentzians may be found in the Appendix. The unfiltered, raw spoke surfaces are shown at the left of each figure, with the typical shared horizontal and angled striations indicating breathing and spoke mode oscillations. According to the PSDs, for both conditions the breathing mode is strongest, followed by the m = 3 spoke mode, then the m = 2 and m = 4 spoke modes, and finally m = 5 the weakest of those shown.

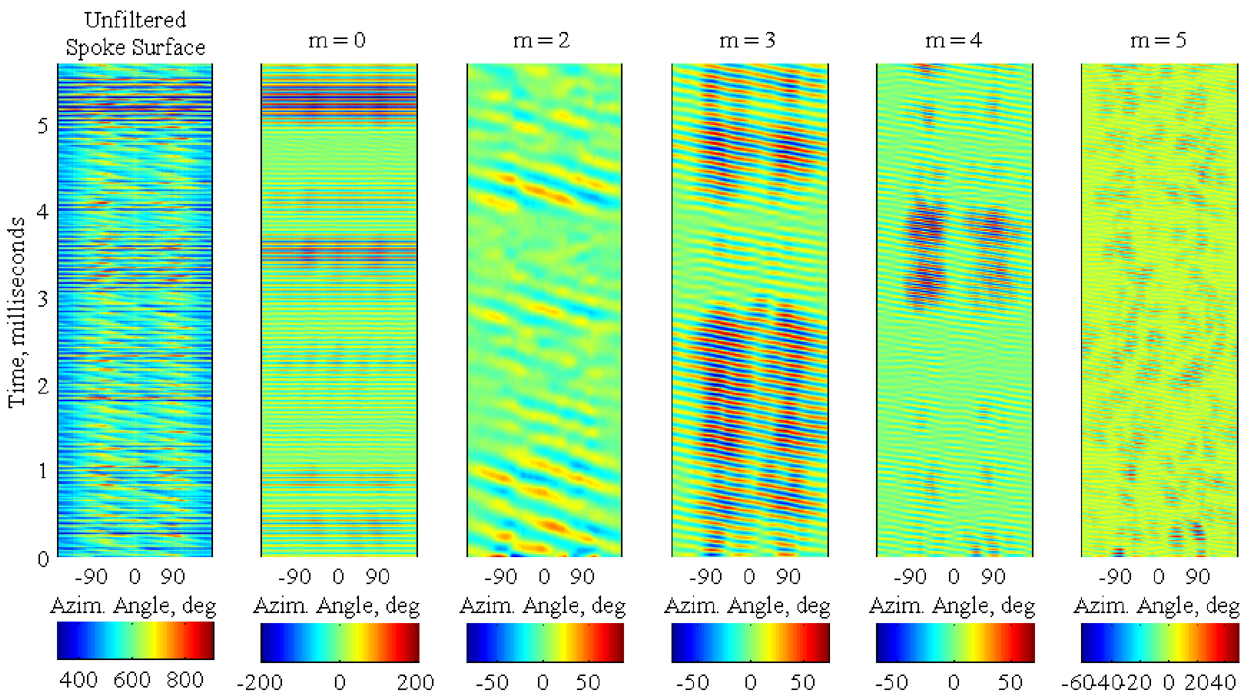

Figure 11. Raw and binwise-filtered spoke surfaces for 400 V, 10 mg/s operating condition from the 'O' parameter sweep. The dominant $m = 3$ and $m = 2$ modes are apparent, with a clear interruption near t = 3.5 ms where the $m = 4$ mode takes over with elevated breathing mode activity. At all times small levels of oscillation are visible for each mode.

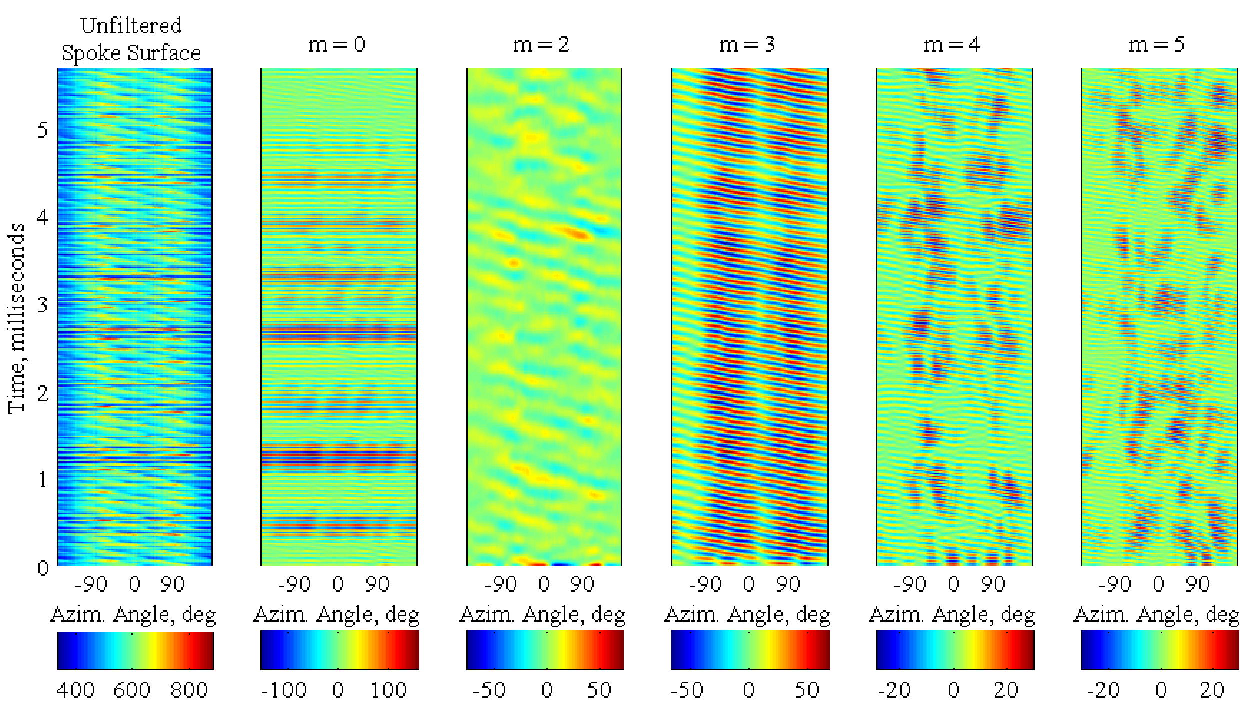

Figure 12. Raw and binwise-filtered spoke surfaces for 600 V, 10 mg/s operating condition from the 'O' parameter sweep.

The second column from left in each figure shows the $m = 0$ breathing mode. Note the purely horizontal striations, indicating uniform oscillation in the azimuth (all around the channel). The breathing mode is not perfectly steady, and over the 5.5 milliseconds shown, both cases show momentary disruptions of a few tenths of a millisecond each where the breathing mode becomes violently oscillatory, before returning to a more stable level. Successive columns from left show successively higher modes, with individual color bars indicating different color scales for each mode. As expected, the $m = 0$ mode shows up with highest amplitude, followed by $m = 3$.

Taken together, these cases and others show that spokes neither completely coexist nor completely segregate, instead residing in a middle state of sometimes coexisting, sometimes trading off. At all times, the several modes show a consistent presence, albeit at a low level for the higher spoke modes. However, on occasion the dominant modes switch up, such as near $t = 3.5$ ms in the 400 V case (Figure 11), when the clear structure of the $m = 3$ mode disappears abruptly and the $m = 4$ mode, largely unnoticed up to that point, grows to dominates the oscillations for the better part of a millisecond. During this interval the breathing mode $m = 0$ also grows. The later surge in the $m = 0$ mode near 5 ms also appears to correspond to a weakening of the $m = 3$ mode.

Using this type of filtering, it may be possible in the future to develop metrics to gauge how steady a particular mode or group of modes are over time, perhaps by measuring cross-correlation with sine waves of $m = 1, 2, 3$ etc. over each filtered video frame in the spoke surface.

V. Conclusions

Previously reported techniques for Fourier analysis of Hall thruster high speed video have been extended here to develop a dimensionless metric for spoke mode strength relative to the breathing mode based on relative amplitude of pixel oscillations. The proposed measure should be generally comparable across videos taken with different cameras of different thrusters in different facilities. A MATLAB toolbox containing the algorithms necessary for video import, Fourier analysis and spoke strength computation has been made open source and publicly available to facilitate such comparisons.

Using the measures of spoke/breathing mode relative strength, several clear trends were observed. Spoke strength becoming strongest relative to the breathing mode near magnetic field strengths optimized to minimize discharge current at a given discharge voltage. For suboptimal $|B|$ in a 300 V discharge, the increase in the spoke/breath ratio is due to decreased breathing mode discharge current oscillations together with a rise in visible spoke strength. For superoptimal $|B|$ at 300 V the decrease in the ratio was due to spoke strength saturating at about 140% of optimal $|B|$ while discharge current oscillations slowly rose again, though not as quickly as in the suboptimal region.

For varied V_D from 105-600 V at fixed $|B|$ optimized for the 300 V case, spoke strength (pixel RMS) increased slightly from 105 - 300 V and weakened slightly from 300-600 V, while breathing mode oscillations decreased more than tenfold from either extreme at 105 or 600 V to a minimum from 300-400 V. Finally, for optimized $|B|$ at V_D from 105 - 600 V, the spoke/breathing mode ratio plateaus at high voltage as both discharge current oscillations drop and stay low while spoke pixel RMS values increase and stay high. Two notable exceptions to these trends are the outlying cases at 150 V, which while they lie on the main sequence appear entirely out of order in the usual progression from low to high voltage.

Careful filtering of spoke surfaces at the frequencies associated with different spoke modes shows that multiple spoke modes can both coexist and in some cases switch abruptly between dominant modes. We confirm results from a previous parameter study that higher spoke modes travel with faster linear velocity (and higher frequency) and that spoke velocity decreases with increasing magnetic field, and report that the spoke velocity asymptotes with increasing mode number in the high 1000 - low 2000 m/s range in the H6 thruster operating on xenon.

VI. Acknowledgments

The Photron SA5 FASTCAM was made available through the support of the Michigan/AFRL Center of Excellence in Electric Propulsion (MACEEP), grant FA9550-09-1-0695, under joint program managers Dr. Mitat Birkan (AFOSR) and Dr. James Haas (AFRL/RZ). The FASTCAM video analysis in this paper was made possible with computing resources funded by a Strategic University Research Partnership (SURP) with the Jet Propulsion Laboratory under principal investigator Dr. Richard Hofer. The first author is grateful for funding support during his graduate work from the National Science Foundation Graduate Research Fellowship Program, the Tau Beta Pi Foundation, the National Defense Industry Association, and the aforementioned SURP.

Appendix A: Data Management, Compression and Minimum Video Length

The videos in this work were all acquired for 1 second for good frequency resolution $\Delta f = 1/\Delta t$ after PSD smoothing, with 256x256 pixels per image for better than 1 mm^2/pixel resolution, and at 87,500 frames per second to capture the breathing mode at well above Nyquist frequency. However, this yielded file sizes of order 10 GB per video. File size for a given video duration, framerate, resolution, and pixel bit depth is given by Eqn. 5

$$\text{File Size } [GB] = (T\ sec)\,(F\ fps)\,(M \times N \frac{pixels}{frame})\left(B \frac{bits}{pixel}\right)\left(\frac{1\ byte}{8\ bits}\right)\left(\frac{1\ GB}{10^9\ bytes}\right) \tag{5}$$

These large file sizes motivate a brief discussion of data management, compression, and minimal video durations necessary for good statistics. Import and storage of videos of GB scale requires a 64-bit memory address space, and Fourier analysis will generally require RAM greater in size than the largest planned video. In practice a margin of at least two is required in RAM using the MATLAB spoke analysis toolkit.[15]

If compression is necessary for permanent data storage, lossless compression preserves information captured in the least significant bits of the image. The Shannon entropy measure of the actual information content[23] of thruster videos averaged about 2 bits per pixel over the parameter study of videos, indicating a theoretical maximum lossless compression ratio of about 80% may be possible. A simple method implemented in the MATLAB toolkit achieves a ~50% lossless compression ratio by applying a 2D Haar transform to each video frame (similar to JPEG compression) and truncating the compressed video to an 8-bit integer data type. Losslessness is maintained at the lower bit depth by separately saving the locations and true values of any truncated pixels (<<1% after 2D Haar transform). Improvements in data storage capacity and affordability may render such compression unnecessary, but for the 25 parameter study videos this saved >100 GB of archived storage space.

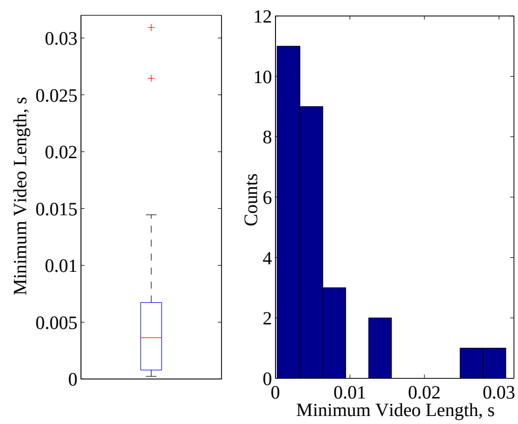

Figure 13. Minimum Video Durations

Another factor allowing reduced data loads is shorter videos. Shorter videos can compute approximate spoke frequencies or the spoke strength metrics of Eqn. 4 with reasonable accuracy. Consider the strength calculated from the full video as the mean μ_0 of strengths calculated from N =1000 1-ms samples. We can also compute the standard deviation σ of the strength over the 1000 samples, and estimate whether a smaller number of samples N_s would have been sufficient to compute a mean strength μ_s with error $E = \mu_s - \mu_0$ less than some threshold, say $E/\mu = 10\%$, at a 95% confidence level as:

$$N_s = \left(\frac{z_{95\%}\frac{\sigma}{\mu}}{E/\mu}\right)^2$$

where $z_{95\%} = 1.6449$ is the z-score for a 95% confidence level. For smaller sample sizes the Student's t-statistic should be used, but for $N = 1000$ the two are nearly identical. For most of the videos in the parameter study $\sigma/\mu < .0X$ when $N = 1000$, giving $N_s < 7$ or minimum video durations of 7 ms. For $E/\mu < 5\%$, $N_s < 27$ for most videos. The distribution of N_s is shown in Figure 13. The outlier is O 150, while the upper extreme in the box plot is V 150. Thus videos as short as 7-27 ms can suffice for diagnosing spoke strengths. Shorter videos also drastically reduce download, import and postprocessing times, enabling high-speed imaging as an on-the-fly diagnostic. Finally, the majority of the variation in videos is due to changes in the breathing mode pixel RMS (see Eqn. 4), so it may be possible to use the discharge current signal directly to estimate the minimum video duration for a desired sampling error.

Appendix B: Collected Parameter Study 2D PSDs

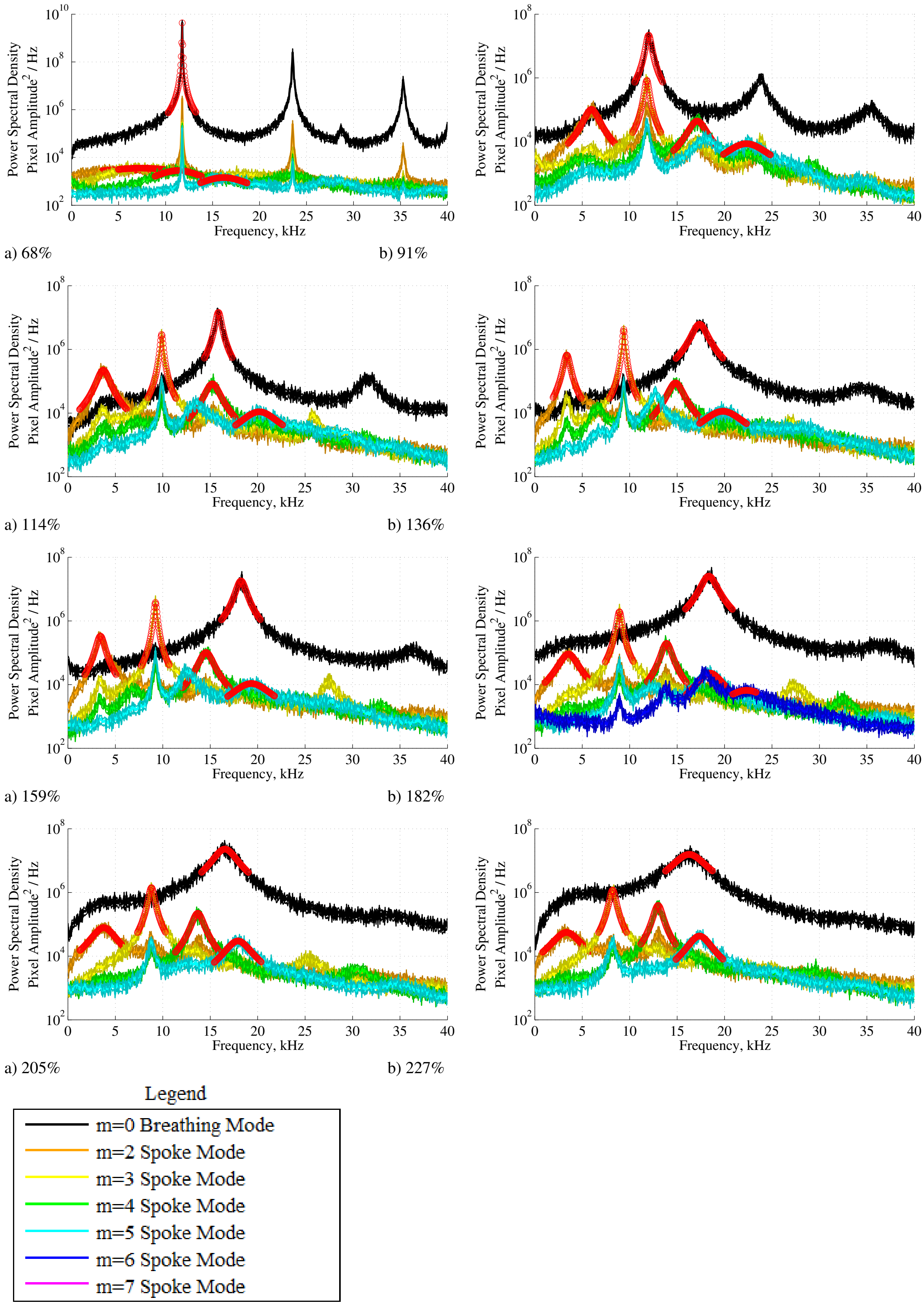

Figure 14. Collected 2D DFTs, Magnetic Field Strength Parameter Sweep 'B' at Fixed 300 V

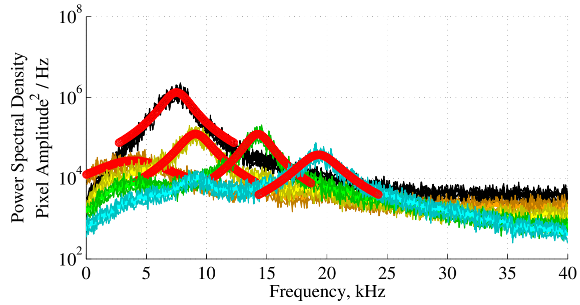

a) 150 V

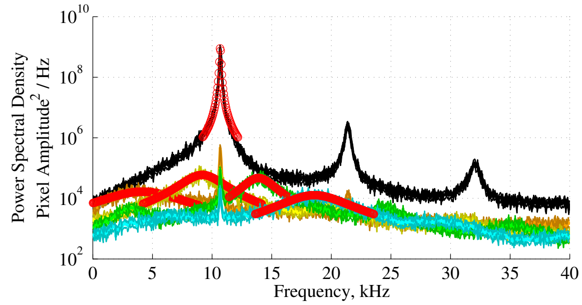

b) 200 V

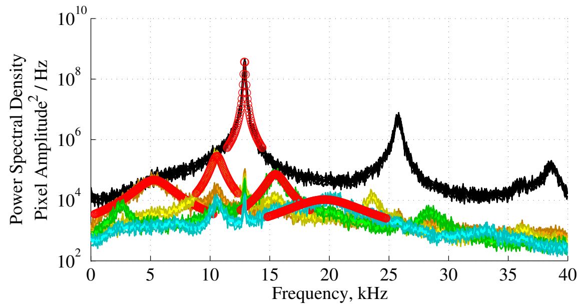

a) 250 V

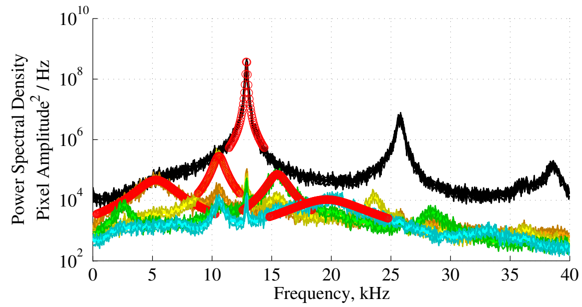

b) 300 V

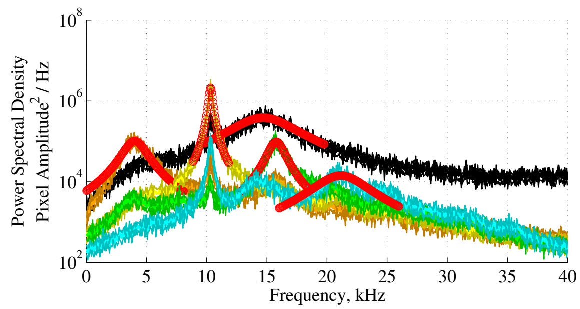

a) 350 V

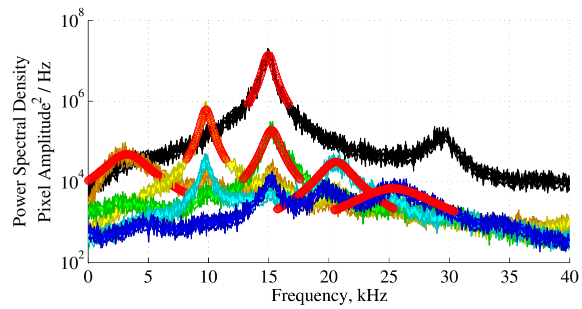

b) 400 V

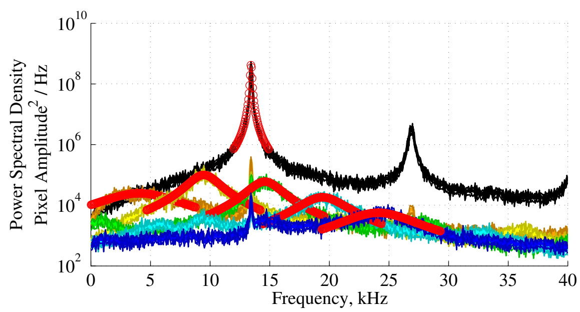

a) 450 V

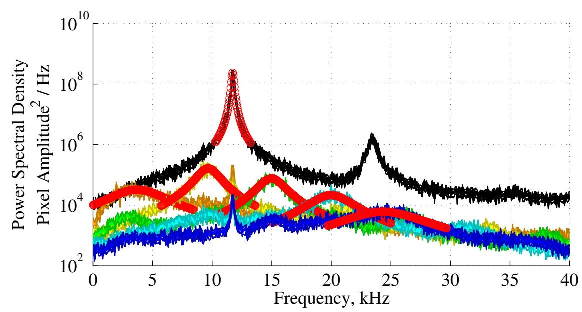

b) 500 V

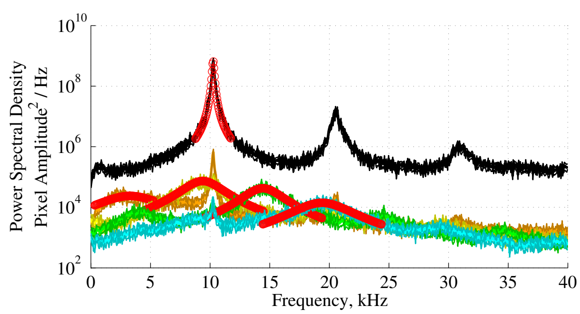

a) 550 V

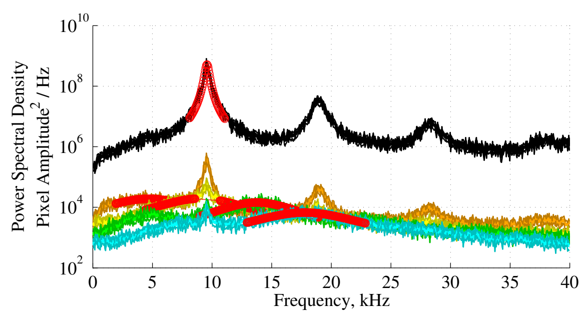

b) 600 V

Figure 15. Collected 2D DFTs, Discharge Voltage Parameter Sweep 'V' at Fixed 101 G Peak Magnetic Field Strength

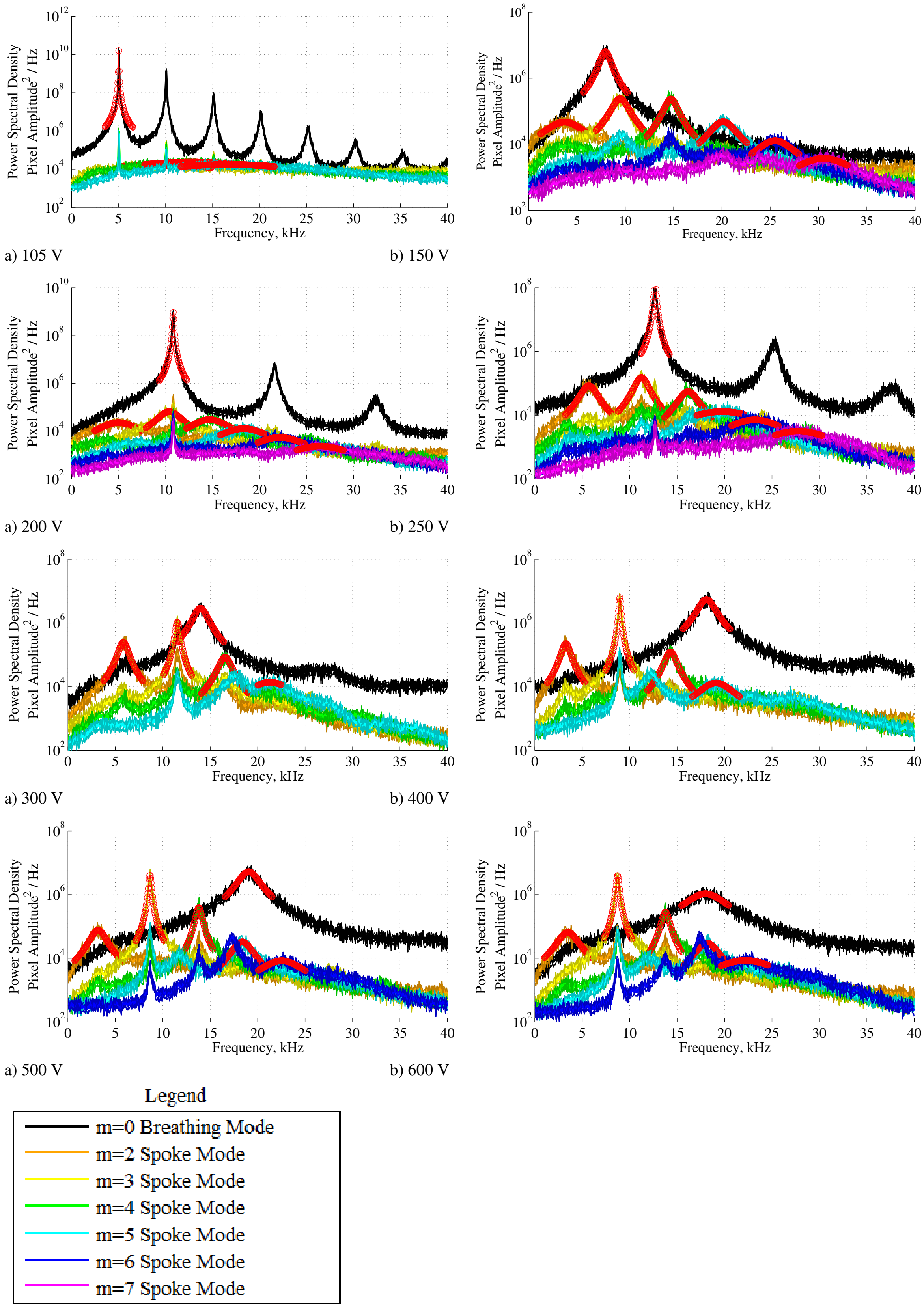

Figure 16. Collected 2D DFTs, Discharge Voltage Parameter Sweep 'O' at Optimized Magnetic Field Strength

References

[1]McDonald, M. S., Sekerak, M. J., Gallimore, A. D., and Hofer, R. R., "Plasma Oscillation Effects on Nested Hall Thruster Operation and Stability," *2010 IEEE Aerospace Conference*, IEEEAC Paper #2502, Big Sky, MT, March 2013, pp. 1 –9.

[2]Florenz, R. F., Gallimore, A., Kamhawi, H., Griffiths, C., Brown, D. L., Hofer, R. R., and Polk, J. E., "First Firing of a 100-kW Nested-channel Hall Thruster," *33rd International Electric Propulsion Conference*, IEPC 2013-394, Washington, DC, USA, 2013.

[3]McDonald, M. S. and Gallimore, A. D., "Measurement of Cross-Field Electron Current in a Hall Thruster Due to Rotating Spoke Instabilities," *47th AIAA/ASME/SAE/ASEE Joint Propulsion Conference & Exhibit*, AIAA 2011-5810, 2011.

[4]McDonald, M. and Gallimore, A., "Parametric Investigation of the Rotating Spoke Instability in Hall Thrusters," *32nd International Electric Propulsion Conference*, IEPC 2011-242, Wiesbaden, Germany, 2011.

[5]McDonald, M. S. and Gallimore, A. D., "Rotating Spoke Instabilities in Hall Thrusters," *IEEE Transactions on Plasma Science*, Vol. 39, No. 11, Nov. 2011, pp. 2952–2953.

[6]Liu, D., Huffman, R. E., Branam, R. D., and Hargus, W. A., "Ultrahigh-Speed Imaging of Hall-Thruster Discharge Oscillations With Krypton Propellant," *IEEE Transactions on Plasma Science*, 2011.

[7]Parker, J. B., Raitses, Y., and Fisch, N. J., "Transition in electron transport in a cylindrical Hall thruster," *Applied Physics Letters*, Vol. 97, No. 9, 2010, pp. 091501.

[8]Ellison, C. L., Raitses, Y., and Fisch, N. J., "Cross-field electron transport induced by a rotating spoke in a cylindrical Hall thruster," *Physics of Plasmas*, Vol. 19, No. 1, Jan. 2012, pp. 013503–013503–7.

[9]Griswold, M. E., Ellison, C. L., Raitses, Y., and Fisch, N. J., "Feedback control of an azimuthal oscillation in the E x B discharge of Hall thrusters," *Physics of Plasmas*, Vol. 19, No. 5, May 2012, pp. 053506–053506–4.

[10]Escobar, D. and Ahedo, E., "Ionization-induced azimuthal oscillation in Hall Effect Thrusters," *32nd International Electric Propulsion Conference*, IEPC 2011-196, Wiesbaden, Germany, 2011.

[11]Escobar, D. and Ahedo, E., "Low-frequency azimuthal stability analysis of Hall thrusters," 2012.

[12]Escobar, D. and Ahedo, E., "Global stability analysis of azimuthal oscillations in Hall Thrsuters," *33rd International Electric Propulsion Conference*, IEPC 2013-304, Washington, DC, USA, 2013.

[13]Fernandez, E., Knoll, A., and Cappelli, M. A., "An axial-azimuthal hybrid simulation of coaxial Hall thrusters," *42nd AIAA/ASME/SAE/ASEE Joint Propulsion Conference & Exhibit*, AIAA 2006-4329, 2006.

[14]Garrigues, L. and Coche, P., "A two dimensional (azimuthal-axial) Particle-In-Cell model of a Hall thuster," *33rd International Electric Propulsion Conference*, IEPC 2013-252, Washington, DC, USA, 2013.

[15]McDonald, M. S., "MATLAB Spoke Analysis Toolkit," http://sourceforge.net/projects/spoketoolbox/, Oct. 2013.

[16]Huang, W., "Spectral results from a xenon Hall thruster," Sept. 2008, Private communication.

[17]McDonald, M. S., *Electron Transport in Hall Thrusters*, Ph.D. thesis, University of Michigan, Ann Arbor, MI, 2011.

[18]Taubin, G., "Estimation of planar curves, surfaces, and nonplanar space curves defined by implicit equations with applications to edge and range image segmentation," *IEEE Transactions on Pattern Analysis and Machine Intelligence*, Vol. 13, No. 11, 1991, pp. 1115–1138.

[19]Kasa, I., "A circle fitting procedure and its error analysis," *IEEE Transactions on Instrumentation and Measurement*, Vol. 25, No. 1, 1976, pp. 8–14.

[20]Chernov, N., *Circular and Linear Regression: Fitting Circles and Lines by Least Squares*, CRC Press, Taylor & Francis Group, Boca Raton, FL, 1st ed., 2011.

[21]French, A. P., *Vibrations and waves*, Norton, New York, 1971.

[22]McDonald, M. S., Liang, R., and Gallimore, A. D., "Practical Application of Wide Bandwidth Floating Emissive Probes and Wavelet Analysis to the X2 Nested Hall Thruster," *33rd International Electric Propulsion Conference*, IEPC 2013-352, Washington, DC, USA, 2013.

[23]Shannon, C. E., "A mathematical theory of communication," *Bell System Technical Journal*, Vol. 27, No. 3, 1948, pp. 379–423.